

Laboratory Exploration of Heat Transfer Regimes in Rapidly Rotating Turbulent Convection

Jonathan S. Cheng,* Matteo Madonia, Andrés J. Aguirre Guzmán, and Rudie P. J. Kunnen
*Fluids & Flows group, Department of Applied Physics and J.M. Burgers Center for Fluid Dynamics,
 Eindhoven University of Technology, P.O. Box 513, 5600 MB Eindhoven, Netherlands*

We report heat transfer and temperature measurements and direct numerical simulations of rapidly rotating convection in water. We achieve unprecedentedly strong rotational influence (Ekman numbers E as low as 10^{-8}). Scaling relations between the heat transfer (Nusselt number Nu) and the strength of thermal forcing (Rayleigh number Ra) demonstrate robust agreement with previous studies, extending those results further in parameter space. Examining the mid-height vertical temperature gradient reveals distinct regime changes of flow phenomenology, coinciding with transitions predicted by asymptotically-reduced simulations. We find a new regime that we refer to as rotationally-influenced turbulence, inaccessible to asymptotics, where rotation is important but not as dominant as in the known geostrophic turbulence regime. The temperature gradients for all E values collapse to a $Ra^{-1/3}$ scaling in this new regime.

Convectively driven, rotationally constrained flows form the basis of many geophysical and astrophysical processes, from dynamo action in the molten iron core of the Earth [1] to atmospheric patterns in gas giants [2]. These systems are massive, complex, and remote from most measurement techniques, such that our understanding of the fluid physics depends on greatly simplified forward models. Much can be learned by distilling the physics down to the canonical problem of rotating Rayleigh-Bénard convection, where a layer of fluid is subject to an unstable vertical temperature gradient and rotates about a vertical axis. Even in this reduced problem, though, vastly different flows emerge depending on the relative strength of rotational and convective forces, and it is imperative that their properties are understood before performing any kind of extrapolation to geophysical settings. Though rotating convection is well-studied at moderate degrees of thermal forcing and rotation in laboratory experiments [3–6] and direct numerical simulations (DNS) [7, 8], a massive parameter gap separates such studies from the extreme conditions associated with planets and stars [9, 10].

Recent studies aiming to bridge this parameter gap have employed large-scale experimental setups [11–14] and high resolution simulations [12, 15–17]. Though gains may appear marginal in the geophysical context, these studies have, in fact, manifested a plethora of novel behaviors not observed in smaller-scale studies. Of particular interest is a range where thermal forcing and rotation both strongly affect the system but neither dominates the other, the regime of so-called “geostrophic turbulence” (GT). Parameter estimates for conditions in planetary fluid layers hint that understanding GT may be the crux to determining how rotating convection models relate to geophysical systems [14, 18].

The regimes of rotating convection are often characterized by relationships between the heat transfer parameters. The Rayleigh number, $Ra = \alpha_T g \Delta T H^3 / \nu \kappa$, describes the magnitude of thermal forcing, where α_T is the coefficient of thermal expansion, g is gravitational acceleration, ΔT is the temperature difference between upper and lower boundaries, H is the height of the fluid layer, ν is the kinematic viscosity, and κ is the thermal diffusivity. Fig. 1a & b visualize the turbulent flows at high Ra values achieved in our experiments. Increasing Ra leads to correspondingly smaller-scale flow structures. The Nusselt number, $Nu = qH/k\Delta T$, describes the efficiency of heat transfer in the system, where q is the heat flux applied to the fluid layer and k is the thermal conductivity of the fluid. $Nu = 1$ indicates pure thermal conduction while $Nu > 1$ indicates the presence of convective heat transport. The Prandtl number $Pr = \nu/\kappa$, which describes the material properties of the fluid, is often fixed at 1 or near 1 in extreme simulations and experiments [13], but can range from ~ 0.1 to 10 in geophysical settings [9]. The heat transfer efficiency forms a power law relationship with the thermal forcing such that $Nu \sim Ra^\gamma$, with distinct values of γ corresponding to distinct behavioral regimes [19, 20].

Rotational influence is represented by the Ekman number $E = \nu/2\Omega H^2$, where Ω is the angular frequency and lower E corresponds to greater rotational constraint. The convective Rossby number $Ro = (RaE^2/Pr)^{1/2}$ is used to compare rotational and convective forces: traditionally, $Ro \lesssim 1$ is “rotationally-affected” while $Ro \gtrsim 1$ is “rotationally-unaffected” [21, 22]. Rotation contributes a vertical ‘stiffness’ to the flow, suppressing the onset of stationary convection to $Ra_C = 8.7E^{-4/3}$ [23] and to the form of cellular structures with horizontal scale $\ell_\nu \sim E^{1/3}H$ [24, 25]. Analogous to nonrotating convection, Nu vs. Ra/Ra_C scaling relationships indicate distinct behavioral regimes.

As visualized in our experiments (see Fig. 1c–f), the

* Current affiliation: Department of Mechanical Engineering, University of Rochester, Rochester, NY 14627, USA

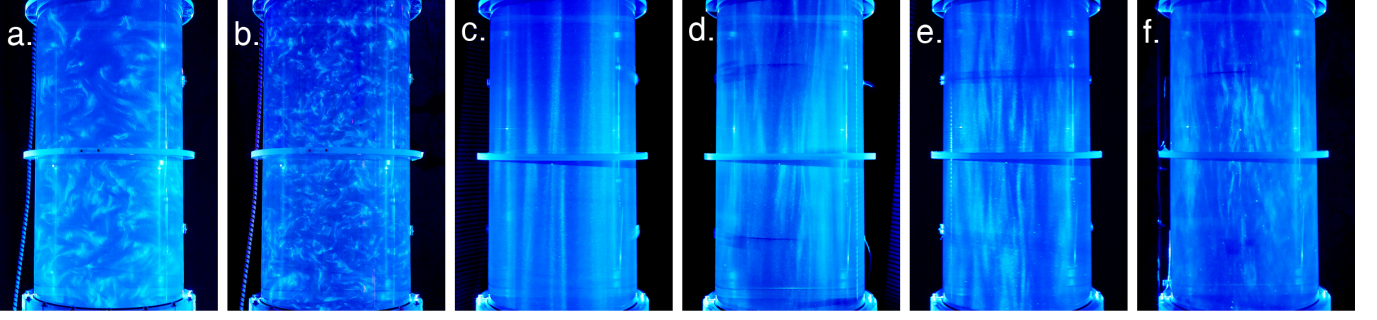


FIG. 1. Visualizations of the flow field in a vertical slice of the $\Gamma = 1/5$ tank. Panels a & b: nonrotating convection at $Ra =$ a) 1.4×10^{11} , b) 2.2×10^{12} . Panels c–f: rotating convection at $E = 5 \times 10^{-8}$ and $Ra =$ c) 9.6×10^{10} (convective Taylor columns), d) 8.6×10^{11} (convective plumes), e) 1.6×10^{12} (geostrophic turbulence), f) 3.3×10^{12} (rotationally-influenced turbulence). The photos are captured by seeding the water with neutrally buoyant rheoscopic particles isolated from shaving cream [26] and illuminating the layer with a vertical laser light sheet.

dominant flow structures evolve as Ra increases relative to Ra_C . Much of our intuition for these structures comes from simulations of the asymptotically-reduced equations, a set of equations rescaled in the limit of infinitely rapid rotation such that $E, Ro \rightarrow 0$ [27]. In the context of asymptotic simulations [18, 28], Ra/Ra_C values correspond to “convective Taylor columns” (panel c) where long, thin structures span the vertical extent of the tank, “convective plumes” (panel d) where the columns begin to laterally interact and become wavy, and GT (panel e), the aforementioned regime where convective forces have destroyed the columnar structure but flows are still constrained to rotational length scales. GT at low E ($\lesssim 10^{-6}$) exists at the limit of accessibility to asymptotic simulations and present-day DNS; it remains largely uncharacterized at $Pr > 1$ and with poorly constrained scaling properties even at $Pr \simeq 1$ [13, 16, 17, 28].

The onset horizontal scale ℓ_ν is believed to accurately describe flows in Fig. 1c–e, and serves as a necessary condition for closure of the asymptotically-reduced equations [27]. This assumption persists until a theoretical upper bound, beyond which buoyancy takes over the horizontal length scale [29, 30]:

$$Ra \sim E^{-8/5} Pr^{3/5}. \quad (1)$$

The final image (panel f) in Fig. 1 lies beyond this upper bound, demonstrating clear differences in flow morphology and setting up another open question: Flows in the realm of $Ro \lesssim 1$ are well-studied at moderate E , but, much as in GT, the behaviors in this range change fundamentally as E decreases. For example, an overshoot in Nu above the nonrotating value is well-documented here [6, 22], but vanishes for $E \lesssim 10^{-6}$, with Nu being suppressed at even lower E [14]. How do we characterize the flows in this range – which we hereon refer to as “rotationally-influenced turbulence” (RIT) – when we lack asymptotic simulations to guide our predictions?

In this study, we analyze 75 new nonrotating and ro-

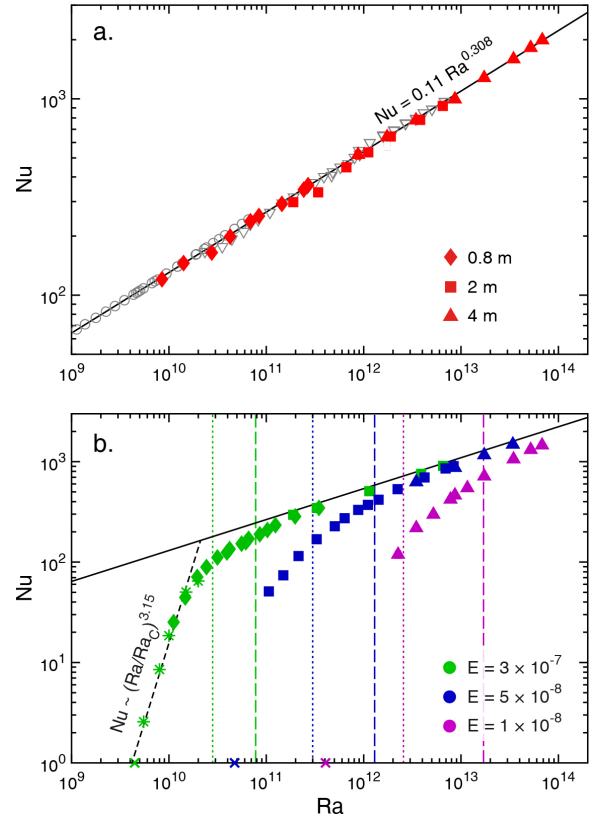


FIG. 2. Nusselt number (Nu) plotted versus Rayleigh number (Ra) for nonrotating convection experimental data (panel a) and rotating convection data (panel b). In both panels, the bullet shape represents tank height H and the solid line represents our best-fit trend in nonrotating convection, $Nu = 0.11 Ra^{0.308}$. The associated aspect ratios for different heights are $\Gamma = 1/2$ for $H = 0.8$ m (diamonds), $\Gamma = 1/5$ for $H = 2$ m (squares), and $\Gamma = 1/10$ for $H = 4$ m (triangles). Data from previous studies are included as open grey circles [31] and triangles [14]. In panel b, the Ekman number (E) is represented by color. Ra_C in each case is indicated by ‘x.’ Numerical simulation cases, included at $E = 3 \times 10^{-7}$, are shown as asterisks. Dotted, color lines represent the predicted transition from convective columns to plumes in [32], while dashed color lines represent the predicted transition from geostrophic turbulence to rotationally-influenced turbulence. A best-fit line through the steep region at $E = 3 \times 10^{-7}$ follows $Nu \sim (Ra/Ra_C)^{3.15}$.

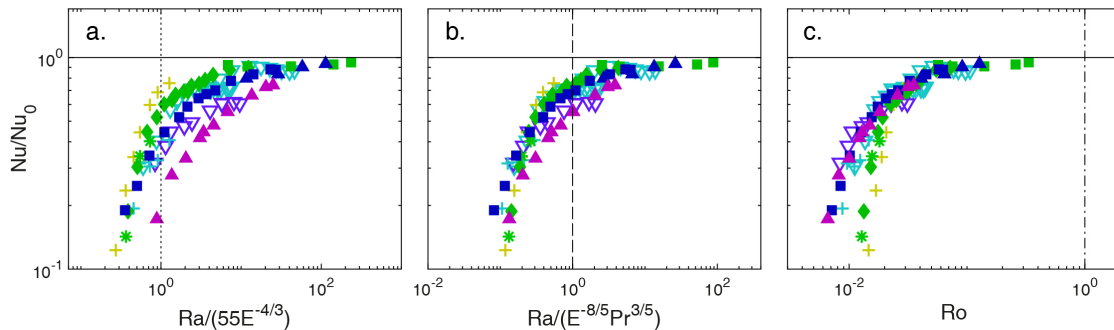


FIG. 3. Nu compensated by nonrotating scaling (2) versus Ra compensated by a) $Ra \sim 55E^{-4/3}$ [32], b) $Ra \sim E^{-8/5}Pr^{3/5}$ [29], and c) $Ra \sim E^{-1}Pr^{1/2}$ ($Ro = 1$) [21]. Bullet color and shape are the same as in Fig. 2, with additional points from [14]: Numerical $E = 1 \times 10^{-6}$ cases are yellow crosses, numerical $E = 1 \times 10^{-7}$ cases are cyan crosses, laboratory $E \simeq 10^{-7}$ cases are empty cyan triangles, and laboratory $E \simeq 3 \times 10^{-8}$ cases are empty indigo triangles.

tating convection data points from the TROCONVEX laboratory setup and from direct numerical simulations, over parameter ranges $10^{10} < Ra < 10^{14}$ and $10^{-8} \leq E \leq 3 \times 10^{-7}$. These data extend the upper bound of Ra by a decade and the lower bound of E by factor of three compared to any previous $Pr > 1$ study. Consistent scaling trends in Nu vs. Ra are observed over a broad range of aspect ratios and between DNS and laboratory experiments, including close agreement with previous work. Near-onset cases undergoing cellular and columnar convection [Fig. 1c] correspond to a steep Nu - Ra scaling, cases far from onset in the RIT regime [Fig. 1f] approach the shallow nonrotating scaling, and in-between cases (plumes, GT) [Fig. 1d & e] follow an intermediate scaling. In contrast to previous work, though, no single transition scaling is found to collapse all of the data.

The reason for this becomes clear when we examine the mean vertical temperature gradient $\partial_z \bar{T}$ across the mid-plane ($z = 0.5$). When plotted against Ra/Ra_C , the temperature gradient undergoes distinct reversals in trend which mark flow regime transitions, in a far clearer way than tracking the Nu - Ra scaling exponent γ . The locations of these reversals correspond closely with transition predictions from asymptotic studies, and they spread apart as E decreases – a behavior that cannot be captured by any single transition scaling. GT manifests as a saturation in the temperature gradient [28] whose parameter range expands as E decreases, and subsequently transitions into RIT in a location that coincides precisely with (1). Scaling Ra by (1) collapses temperature gradient data across all E values into a single trend, indicating a previously unobserved, but robust mode of heat transport in this regime.

Laboratory data are acquired from TROCONVEX: a large-scale rotating convection device at Eindhoven University of Technology. In order to access broad ranges of Ra and E , interchangeable tanks of height $H = 0.8, 2$, and 4 m but equal diameter $D = 0.39$ m are used (always satisfying $\Gamma > 10\ell_\nu/H$ [33]). Temperatures are

measured via resistance thermistors embedded in the top, bottom, and sidewall of these tanks within 0.7 mm of the fluid layer. Top and bottom thermistors give the overall temperature gradient needed to calculate the globally-averaged heat transfer parameters Nu and Ra . Sidewall thermistors are embedded two at each height, opposite each other on the cylindrical sidewall, over multiple tank heights. Further measurement details can be found in the Supplement [34]. The working fluid is water at a mean temperature of about 31°C , corresponding to $Pr = 5.2$. Numerical simulations are necessary to bridge the gap between laboratory experimental data and the onset of convection, where the minute temperature differences required cannot be stably maintained in the lab [12, 33]. DNS runs are conducted at $E = 3 \times 10^{-7}$, $Pr = 5.5$ in a $384 \times 384 \times 640$ cell cartesian grid of aspect ratio $\Gamma = 10\ell_\nu/H = 0.323$ (horizontal dimensions are each of size $10\ell_\nu$). The temperature field is resolved on a grid refined by a factor of 2 in both horizontal directions. Non-slip and constant-temperature conditions apply at the top and bottom boundaries, while horizontal boundary conditions are periodic. For further information about the code, see [35]. All experimental and numerical data points are tabulated in the Supplement [34].

Fig. 2 presents our data in terms of the relationship between Nu and Ra . Our nonrotating data in Fig. 2a follow a best-fit scaling of

$$Nu_0 = 0.11 \left(\begin{smallmatrix} +0.02 \\ -0.01 \end{smallmatrix} \right) Ra^{0.308 \pm 0.005}, \quad (2)$$

agreeing with previous scaling trends of $\sim 0.3 - 0.33$ found in water [14, 36, 37] and in other media [38–40]. It is also consistent with the classical prediction that $Nu \sim Ra^{1/3}$ when the bulk is sufficiently turbulent as to be approximately isothermal, with the temperature gradient confined entirely to the upper and lower thermal boundary layers [19]. There is no evidence of a transition to a steeper scaling that would indicate the ultimate regime of RBC [20, 41], though this may be because of the narrow geometry employed ($\Gamma \leq 1/2$). Ro-

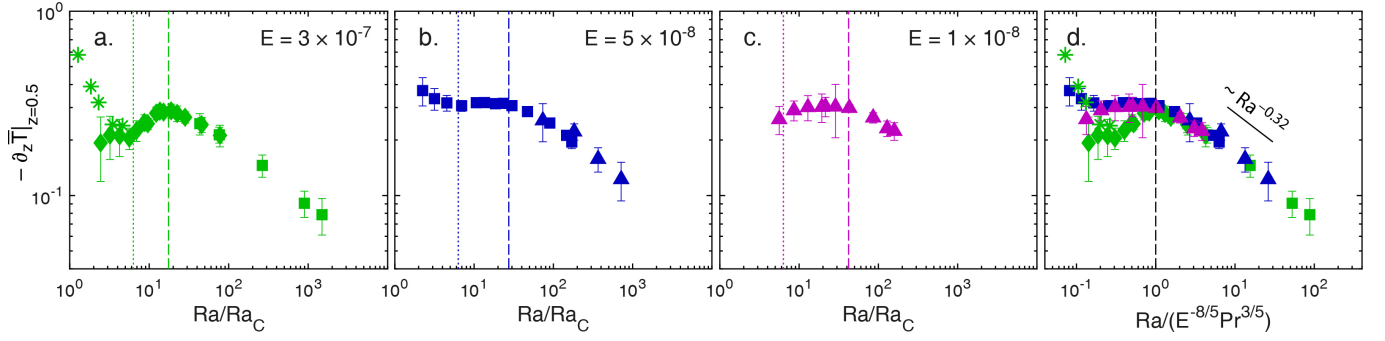


FIG. 4. Normalized mid-height temperature gradient $-\partial_z \bar{T}|_{z=0.5}$ plotted versus Ra/Ra_C for a) $E = 3 \times 10^{-7}$, b) $E = 5 \times 10^{-8}$, and c) $E = 1 \times 10^{-8}$. Symbol shapes correspond to tank aspect ratio, as in Fig. 2. Dotted lines represent Eq. (3); dashed lines Eq. (1). d) Normalized mid-height temperature gradient $-\partial_z \bar{T}|_{z=0.5}$ plotted versus Ra compensated by (1) for data at all three E values combined. A best-fit scaling across all E values beyond the transition produces a trend of $-\partial_z \bar{T}|_{z=0.5} \sim Ra^{-0.32}$.

tating data plotted in Fig. 2b show a characteristically steep slope near onset which flattens toward the nonrotating scaling (2) as Ra increases relative to Ra_C . For $E = 3 \times 10^{-7}$, we observe robust agreement between simulations (with periodic boundary conditions) and laboratory experiments (in a narrow tank with non-slip boundaries). Plotting a best-fit trend for points in the cellular and columnar regime gives $Nu \sim (Ra/Ra_C)^{3.15 \pm 0.15}$, consistent with scalings found in other low- E , $Pr \simeq 3$ –10 studies [12, 14, 16]. As is characteristic for very low E , rotational Nu values lie below the nonrotating Nu_0 values until well beyond onset. This separation becomes more pronounced as E decreases: the $E = 3 \times 10^{-7}$ trend first comes within 10% of the nonrotating trend at $Ra/Ra_C = 43$, while for $E = 5 \times 10^{-8}$ this does not occur until $Ra/Ra_C = 370$. This seems to indicate that the range of GT expands as E is lowered, although predicted regime transitions (marked by dotted and dashed lines in Fig. 2b) only roughly map out changes in the Nu – Ra scaling, whose evolution apparently lacks sharp transitions.

This smoothness is further evident in Fig. 3, where Nu is compensated by the best-fit nonrotating scaling trend Nu_0 defined by (2), and Ra is compensated by several different transition arguments. In contrast to previous studies, it is not clear that any of these arguments definitively collapse data over multiple E values [13, 14]. Fig. 3a compensates Ra by an asymptotic prediction for the transition from columnar convection to plumes [32]:

$$Ra = 55E^{-4/3}, \quad (3)$$

but gives little evidence of collapse. Fig. 3b shows that compensating with (1) collapses the near-onset trends while inducing some spread in the GT range, while Fig. 3c shows that compensating by Ro does the opposite. In Fig. 3c, it can be seen that all of our data exist well before the $Ro_C = 1$ transition marking the onset of nonrotating-style convection [21, 22]. The visualization in Fig. 1f

confirms that rotational effects are still felt by the flow when Nu approaches Nu_0 , but the gradual shifts in Nu do little to characterize the flow physics.

In lieu of detailed transition information from the globally-averaged parameters, we turn our focus to the mean vertical temperature gradient $-\partial_z \bar{T}|_{z=0.5}$. For our nonrotating convection cases, the temperature profile is sharply divided between the bulk, which is nearly isothermal ($-\partial_z \bar{T} \approx 0$), and the thermal boundary layers, within which nearly all of the temperature drop ΔT occurs [20, 42]. However, in rotating convection, the shape of the temperature profile evolves as Ra/Ra_C increases and the flow morphology changes. The portion of the temperature gradient partitioned to the bulk likewise evolves, giving it the diagnostic properties we seek [17, 28, 32].

Fig. 4a–c shows that the temperature gradient measured at tank mid-height, $-\partial_z \bar{T}|_{z=0.5}$, is indeed a robust tool for determining regime transitions at each E value (information on how $-\partial_z \bar{T}|_{z=0.5}$ and associated error bars are calculated from raw temperature data can be found in the Supplement [34]). In the cellular and columnar regimes, increasing Ra leads to a decreasing temperature gradient. At (3) this trend reverses, indicating that increasing Ra now forces more of the temperature gradient into the interior as the horizontal rigidity of bulk flow structures relaxes. Visualizations of the flow and Nu – Ra data do not make it clear where the plumes-to-GT regime transition takes place. However, asymptotic studies posit that GT corresponds to $-\partial_z \bar{T}|_{z=0.5}$ flattening with increasing Ra/Ra_C [28]. Qualitatively, our results do appear to manifest such a flattening at $Ra/Ra_C \simeq 15$ at each E value. This abruptly gives way to a decreasing trend at (1), where the flow enters the RIT regime. As (1) and (3) are separated by a factor of $E^{4/15}$, the parameter range of GT evidently increases as E decreases toward geophysical values.

In Fig. 4d we compile the $-\partial_z \bar{T}|_{z=0.5}$ data for all E values and plot them versus Ra rescaled by (1). All data

to the right of the dashed line, then, lie in the RIT regime. Overplotting separate E trends collapses all data in this regime into an approximate $-\partial_z \bar{T}|_{z=0.5} \sim Ra^{-1/3}$ scaling. We speculate that thermal boundary layers of the nonrotating style have formed beyond this transition, such that increasing Ra causes stronger mixing in the bulk and isolates more of the temperature gradient into the boundary layers. This scaling exponent is, to the best of our knowledge, a novel result in rotating convection, and the fact that it has not been observed in higher E ranges reinforces the idea that the traditional understanding of the “rotationally-affected” regime no longer applies to its low- E analogue, the RIT regime.

Our novel survey of rotating convection cases demonstrates the emergence of several distinct regimes as E is pushed lower than any previous study in water. Agreements between DNS and laboratory cases and between tanks of differing aspect ratio are found for all diagnostic methods. The Nu – Ra scaling exponent γ demonstrates strong consistency with previous results while extending them to more extreme parameter ranges. However, it is not useful for determining precise transition locations. The mid-height temperature gradient $-\partial_z \bar{T}|_{z=0.5}$ provides a robust measure in this regard: transitions that are nigh invisible in Nu – Ra and compensated Nu – Ra plots [Figs. 2 & 3] are distinctly expressed as reversals in the trend of $-\partial_z \bar{T}|_{z=0.5}$ vs. Ra/Ra_C [Fig. 4]. Through this method, we confirm that the range of geostrophic turbulence expands as E decreases. We also encounter the existence of a rotationally-influenced turbulence regime for $Ra > E^{-8/5} Pr^{3/5}$, analogous to the rotationally-affected regime of moderate E [6, 22], but containing novel behaviors. Within this regime, data over all E values collapse as $-\partial_z \bar{T}|_{z=0.5} \sim Ra^{-1/3}$. This decreasing trend expresses how thermal gradients are funneled into the boundary layers with increasing Ra .

Much like how the classical dichotomy of “rotationally-dominated” vs. “rotationally-affected” convection breaks down with increasing rotation, our results make it clear that the subsequent inclusion of geostrophic turbulence as an intermediate regime is also limited in scope. Instead, while the GT regime does exist and continue to expand, the apparent majority of Ra/Ra_C space prior to nonrotating-style convection is occupied by rotationally-influenced turbulence. If we extrapolate the asymptotic arguments supported in this paper, the gaps between each regime transition widen as E decreases: the plumes / GT range expands as $Ra \sim E^{4/15}$ while the RIT range expands as $Ra \sim E^{2/5}$. In the geophysical context, estimates for fluid layers in solar system planets place E around $\sim 10^{-19} - 10^{-12}$ [9], with $Ra/Ra_C \sim 10^2 - 10^3$ [43]. Rotating convection in these layers would then invariably inhabit either geostrophic turbulence or rotationally-influenced turbulence. Though such an analysis is certainly too simplistic to capture the complex flows in planets, it reinforces that the relevant physics

are not likely to exist in classical models for rotating convection. This work provides a significant step toward developing new models for geophysically-relevant regimes of rotating convection.

The authors have received funding from the European Research Council (ERC) under the European Union’s Horizon 2020 research and innovation programme (Grant agreement No. 678634). We are grateful for the support of the Netherlands Organisation for Scientific Research (NWO) for the use of supercomputer facilities (Cartesius) under Grants No. 15462, 16467 and 2019.005.

-
- [1] G. A. Glatzmaier and P. H. Roberts, *Phys. Earth Planet. Inter.* **91**, 63 (1995).
 - [2] M. Heimpel, J. Aurnou, and J. Wicht, *Nature* **438**, 193 (2005).
 - [3] H. T. Rossby, *J. Fluid Mech.* **36**, 309 (1969).
 - [4] Y. Liu and R. E. Ecke, *Phys. Rev. Lett.* **79**, 2257 (1997).
 - [5] R. P. J. Kunnen, H. J. H. Clercx, and B. J. Geurts, *EPL (Europhysics Letters)* **84**, 24001 (2008).
 - [6] J.-Q. Zhong, R. J. A. M. Stevens, H. J. H. Clercx, R. Verzicco, D. Lohse, and G. Ahlers, *Phys. Rev. Lett.* **102**, 044502 (2009).
 - [7] K. Julien, S. Legg, J. McWilliams, and J. Werne, *J. Fluid Mech.* **322**, 243 (1996).
 - [8] S. Schmitz and A. Tilgner, *Phys. Rev. E* **80** (2009).
 - [9] G. Schubert and K. M. Soderlund, *Phys. Earth Planet. Inter.* **187**, 92 (2011).
 - [10] P. H. Roberts and E. M. King, *Rev. Prog. Phys.* **76**, 096801 (2013).
 - [11] S. Weiss and G. Ahlers, *J. Fluid Mech.* **684**, 407 (2011).
 - [12] E. M. King, S. Stellmach, and J. M. Aurnou, *J. Fluid Mech.* **691**, 568 (2012).
 - [13] R. E. Ecke and J. J. Niemela, *Phys. Rev. Lett.* **113**, 114301 (2014).
 - [14] J. S. Cheng, S. Stellmach, A. Ribeiro, A. Grannan, E. M. King, and J. M. Aurnou, *Geophys. J. Int.* **201**, 1 (2015).
 - [15] B. Favier, L. J. Silvers, and M. R. E. Proctor, *Phys. Fluids* **26**, 096605 (2014).
 - [16] S. Stellmach, M. Lischper, K. Julien, G. Vasil, J. S. Cheng, A. Ribeiro, E. M. King, and J. M. Aurnou, *Phys. Rev. Lett.* **113**, 254501 (2014).
 - [17] R. P. J. Kunnen, R. Ostilla-Mónico, E. P. van der Poel, R. Verzicco, and D. Lohse, *J. Fluid Mech.* **799**, 413 (2016).
 - [18] J. M. Aurnou, M. A. Calkins, J. S. Cheng, K. Julien, E. M. King, D. Nieves, K. M. Soderlund, and S. Stellmach, *Phys. Earth Planet. Inter.* **246**, 52 (2015).
 - [19] W. V. Malkus, *Proc. Roy. Soc. Lond. A* **225**, 196 (1954).
 - [20] G. Ahlers, S. Grossman, and D. Lohse, *Rev. Mod. Phys.* **81**, 503 (2009).
 - [21] P. A. Gilman, *Geophys. Astrophys. Fluid Dyn.* **8**, 93 (1977).
 - [22] R. J. A. M. Stevens, H. J. H. Clercx, and D. Lohse, *Eur. J. Mech. B/Fluids* **40**, 41 (2013).
 - [23] S. Chandrasekhar, *Hydrodynamic and Hydromagnetic Stability*, 1st ed. (Oxford University Press, 1961).
 - [24] K. Zhang and G. Schubert, *Ann. Rev. Fluid Mech.* **32**, 409 (2000).

- [25] S. Stellmach and U. Hansen, Phys. Rev. E **70**, 056312 (2004).
- [26] D. Borrero-Echeverry, C. J. Crowley, and T. P. Riddick, Phys. Fluids **30**, 087103 (2018).
- [27] M. Sprague, K. Julien, E. Knobloch, and J. Werne, J. Fluid Mech. **551**, 141 (2006).
- [28] K. Julien, A. M. Rubio, I. Grooms, and E. Knobloch, Geophys. Astrophys. Fluid Dyn. **106**, 254503 (2012).
- [29] K. Julien, E. Knobloch, A. M. Rubio, and G. M. Vasil, Phys. Rev. Lett. **109**, 254503 (2012).
- [30] T. Gastine, J. Wicht, and J. Aubert, J. Fluid Mech. **808**, 690 (2016).
- [31] D. Funfschilling, E. Brown, A. Nikolaenko, and G. Ahlers, J. Fluid Mech. **536**, 145 (2005).
- [32] D. Nieves, A. M. Rubio, and K. Julien, Phys. Fluids **26**, 086602 (2014).
- [33] J. S. Cheng, J. M. Aurnou, K. Julien, and R. P. J. Kunnen, Geophys. Astrophys. Fluid Dyn. **112**, 277 (2018).
- [34] See Supplemental Material at [url], which includes Refs. [44–50], for description of the experimental apparatus, measurement techniques, error analysis, additional figures, and data tables.
- [35] R. Ostilla-Monico, Y. Yang, E. P. van der Poel, D. Lohse, and R. Verzicco, J. Comput. Phys. **301**, 308 (2015).
- [36] E. Brown, A. Nikolaenko, D. Funfschilling, and G. Ahlers, Phys. Fluids **17**, 075108 (2005).
- [37] C. Sun, L.-Y. Ren, H. Song, and K.-Q. Xia, J. Fluid Mech. **542**, 165 (2005).
- [38] J. J. Niemela, L. Skrbek, K. R. Sreenivasan, and R. J. Donnelly, Nature **404**, 837 (2000).
- [39] D. Funfschilling, E. Bodenschatz, and G. Ahlers, Phys. Rev. Lett. **103**, 014503 (2009).
- [40] J. J. Niemela, S. Babuin, and K. R. Sreenivasan, J. Fluid Mech. **649**, 509 (2010).
- [41] R. H. Kraichnan, Phys. Fluids **5**, 1374 (1962).
- [42] S. Grossmann and D. Lohse, J. Fluid Mech. **407**, 27 (2000).
- [43] J. S. Cheng and J. M. Aurnou, Earth Planet. Sci. Lett. **436**, 121 (2016).
- [44] G. V. Bayley and J. M. Hammersley, J. R. Stat. Soc. Suppl. **8**, 184 (1946).
- [45] J. Taylor, *Introduction to Error Analysis, The Study of Uncertainties in Physical Measurements*, 2nd ed. (University Science Books, 1997).
- [46] D. R. Lide, *CRC Handbook of Chemistry and Physics: A Ready-Reference Book of Chemical and Physical Data: 2003–2004* (CRC Press, 2003).
- [47] E. Brown and G. Ahlers, Europhys. Lett. **80**, 14001 (2007).
- [48] R. P. J. Kunnen, B. J. Geurts, and H. J. H. Clercx, J. Fluid Mech. **642**, 445 (2010).
- [49] A. Zięba and P. Ramza, Metrol. Meas. Syst. **18**, 529 (2011).
- [50] S. Horn and J. M. Aurnou, Phys. Rev. Fluids **4**, 073501 (2019).